pp. 1–25 (2024)

Towards realistic blood cell biomechanics in microvascular thrombosis simulations

A. V. Belyaev[a]

Abstract — The paper is devoted to a three-dimensional mesoscale hemodynamic model for simulations of microvascular blood flows at cellular resolution. The focus is on creating a more accurate biomechanical model of red blood cells for further use in models of hemostasis and thrombosis. The presented model effectively and accurately reproduces peculiarities of blood flow under realistic hydrodynamic conditions in arterioles, venules, and capillaries, including the Fahraeus–Lindquist effect and subsequent platelet margination. In addition, shear-dependent platelet aggregation can also be captured using the proposed approach.

Keywords: Hemodynamics, computer simulations, lattice Boltzmann method, physiological flows, platelet adhesion

MSC 2010: 92C35, 76Z05

Hemodynamic modelling nowadays is one of the well-established theoretical approaches for biomedical research of physiological flows. It includes diverse variants of computational approaches applied to the blood flows in vivo and in vitro: computational fluid dynamics, particle dynamics, kinetic and stochastic modelling, cellular automata, etc. [10, 65, 24, 68].

There are several degrees of spacial detalization of blood in these mathematical models, depending on the particular phenomena of interest. For instance, the lumped-parameter models give a simplified representation of the circulatory system by its equivalence to the electrical circuits, due to the linear flow rate-pressure relation of Hagen–Poiseuille law. Advanced low-dimensional mathematical models of the blood circulatory system account for the transient flows, vessel elasticity, turbulence and non-Newtonian rheology of blood, thus giving an efficient tool for blood flow simulations on a macroscopic length scale, such as whole organism or anatomic compartments [3, 55, 54].

Other classes of problems address local phenomena in blood vessels and thus require modelling approaches that operate at smaller length scales, reaching the cellular and even the molecular level of biophysical details [23, 42, 12, 61, 22]. Many processes in blood vessels, such as thrombosis and hemostasis, rely on biomechanical (rheological) and biochemical effects that are multi-scale by their nature.

[a]M. V. Lomonosov Moscow State University, Faculty of Physics, 1 Leninskiye Gory, 119991 Moscow, Russia. E-mail: aleksey_belyaev@physics.msu.ru

This research was supported by the Russian Science Foundation, grant No. 24-21-00182.

The historical experiments of Fahraeus and Lindquist suggest that in narrow tubes ($< 100\mu$m) the apparent relative viscosity of blood depends on the tube diameter [21]. It is also known that platelet collisions with red blood cells provide their transport to the vessel walls and promote their adhesion to injuries [59, 60]. Apparently fluid mechanics plays a crucial role in thrombogenesis [5, 46, 26, 44]. Concentrations of cells, their collisions and aggregation, drag forces, shear rates and flow velocities, rheology, as well as mechano-sensitivity and conformational changes of proteins should be taken into account in models of arterial and microvascular thrombosis [56, 50, 59, 60, 38, 9]. Therefore, a numerical approach that is capable of accounting for all the biomechanical details of blood flow at molecular and cellular scales is tremendously important for thrombosis and hemostasis modelling.

This paper addresses some issues related to 3D computer simulations of blood flows and thrombosis in microvasculature. The study uses a cell-resolving biomechanical approach implemented as a hybrid model that combines continuum representation for the fluid (blood plasma) and particle dynamics for the blood cells, as well as the proteins involved in thrombosis. The main goal of the present paper is to modify the existing mechanical model of red blood cells, to validate the new model against the experimental data, and to demonstrate its capabilities for computational study of shear-induced platelet aggregation and thrombosis in arterioles, venules and capillaries.

1. Materials and methods

By means of 3D computer simulations the present paper investigates a pressure-driven flow of a dense suspension of red blood cells (RBCs), blood platelets and von Willebrand factor (VWF) in a cylindrical microtube. The recruitment of platelets to the wall-bound von Willebrand factor multimers was inspected as a model of thrombosis in inflamed microvessel [48].

The simulations are carried out in a rectangular box $b_x \times b_y \times b_z$ filled with a viscous fluid. A cylindrical pore is introduced to imitate the internal space of a blood vessel (see Fig. 1). The main axis of the pore was oriented in the x-direction of the simulation box. The inner volume of the pore is available for the cells and the fluid. The walls are meant to be impenetrable for particles and the fluid. Besides that, the hydrodynamic no-slip condition is also introduced at the vessel walls. At $x = 0$ and $x = b_x$ the periodic boundary conditions are imposed for both particles and fluid, while the pressure gradient along the x-direction was established as an external body force exerted on the fluid. In addition, an auxillary setup corresponding to plane shear flow is used for validations and tests. In this case constant fluid velocity is imposed on the solid walls located at $z = 0$ and $z = b_z$, periodic conditions — at other boundaries, and the external pressure gradient is set to zero.

The blood cells (platelets and RBCs) were also introduced explicitely as deformable objects that were able to interact with each other, with polymers and with the fluid. The physical model of these interactions was governed by a set of prescribed forces and constraints. The numerical method was based on a combination

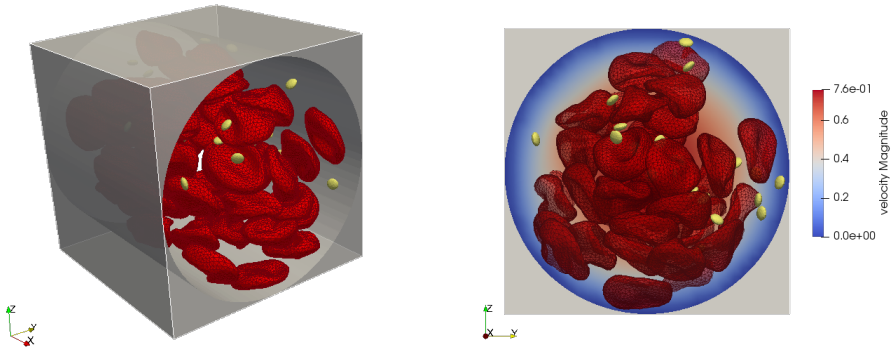

Figure 1. Geometry used in simulations for the pressure-driven (Poiseuille) flow: 3D view (left) and front view (right). The grey parts correspond to solid, impenetrable walls and represent the geometrical constraints. A cylindrical x-oriented pore representing the internal space of a blood vessel was introduced in the simulation box. The colour mapping on the right indicates (as an example) that velocity magnitude is zero at the inner walls of the pore.

of the Lattice Boltzmann method (LBM) [58] with the Particle Dynamics (PD) [18]. The model consists of three principal components: viscous fluid (blood plasma), blood cells and the von Willebrand factor multimers (polymers). The description of each component is presented further in this section. In most of the simulations the following scales for length, force and time were used: $[L] = 10^{-6}$ m, $[F] = 10^{-9}$ N, $[t] = 10^{-4}$ s. The physical parameters were non-dimensionalized according to this system of units. The time step for particle dynamics for most of the presented computations was set $\Delta t_p = 0.0025[t]$ to achieve a balance between efficiency and numerical stability. The model allows for multi-time-step integration, $\Delta t_{LB} = N\Delta t_p$, however for accuracy $N = 1$ in all presented computations. The simulation runs with a smaller step $\Delta t_p = 0.002[t]$ demonstrated no significant changes in system dynamics.

Before each simulation run, a certain number of VWF multimers was attached to the inner surface of the tube. The same amount of VWF multimers was freely suspended in the fluid. Then polymer-fluid system was equilibrated. After that the blood cells were placed in a simulation box at certain locations inside the pore, and the simulation started. The blood vessel radius, the number of VWF multimers, as well as the number of cells was varied during this study.

1.1. Fluid model

Continuum representation was used for the modelling of blood plasma, and Lattice Boltzmann method (LBM) was used to calculate fluid velocity in the simulation box. LBM is used as a fast solver for hydrodynamic equations, that inherits from lattice gas automata simulations [58]. The method rests upon the Boltzmann kinetic equation that describes spacial-temporal changes of a one-particle distribution

function $f(\mathbf{x},\mathbf{u},t)$:

$$\frac{\partial f}{\partial t}+\mathbf{u}\cdot\frac{\partial f}{\partial \mathbf{x}}+\frac{\mathbf{F}}{m}\cdot\frac{\partial f}{\partial \mathbf{u}}=-\frac{f-f^{\mathrm{eq}}}{\tau} \tag{1.1}$$

where the term in the right hand side is the collision integral in Bhatnagar–Gross–Krook form.

A discretization scheme D3Q19 has been used in this work, i.e., the fluid is treated as packets of fluid particles moving from one node to a neighbouring node of a 3-dimensional periodic cubic grid in 19 possible directions. A regular cubic grid of Eulerian spatial sites $\{\mathbf{x}\}$ with constant spacing $\Delta x=[L]$ was introduced, as well as a set of discrete microscopic velocities $\{\mathbf{c}_i\}$. The following notation is conventionally used $f_i(\mathbf{x},t)\equiv f(\mathbf{x},\mathbf{c}_i,t)$ and

$$\mathbf{c}_i=c\times\begin{cases}(0,0,0), & i=0\\ (\pm1,0,0),(0,\pm1,0),(0,0,\pm1), & i=1,2,...,6\\ (\pm1,\pm1,0),(0,\pm1,\pm1),(\pm1,0,\pm1), & i=7,8,...,18\,.\end{cases} \tag{1.2}$$

The discretized function $f_i(\mathbf{x},t)$ obeys the following equation in the case of the thermalized fluid [18, 57, 31, 1]:

$$f_i(\mathbf{x}+\mathbf{c}_i\Delta t,t+\Delta t)-f_i(\mathbf{x},t)=-\frac{\Delta t}{\tau}\left[f_i(\mathbf{x},t)-f_i^{\mathrm{eq}}(\mathbf{x},t)\right]+\Delta t\cdot F_i(\mathbf{x},t)+\chi_i(\mathbf{x},t), \tag{1.3}$$

and the evolution of the system could be found by consequent iterations. For setting up the no-slip hydrodynamic boundaries the 'bounce back' method is used [18].

The equilibrium distribution function $f_i^{\mathrm{eq}}(\mathbf{x},t)$ corresponds to the series expansion of Maxwell-Boltzmann distribution for small velocities [58, 14]. The relaxation time τ is related to the kinematic viscosity of the fluid $\nu=c_s^2(\tau-\Delta t/2)$ and the lattice speed of sound c_s^2. The forcing term $F_i(\mathbf{x},t)$ accounts for any external forces on the fluid, including particle-to-fluid coupling forces:

$$F_i(\mathbf{x},t)=\left(1-\frac{\Delta t}{2\tau}\right)w_i\left[\frac{\mathbf{c}_i-\mathbf{u}}{c_s^2}+\frac{\mathbf{c}_i\cdot\mathbf{u}}{c_s^4}\mathbf{c}_i\right]\cdot\mathbf{F} \tag{1.4}$$

where $\mathbf{F}$ is the body force density, the normalized weights $\{w_i\}$ correspond to the chosen velocity set $\{\mathbf{c}_i\}$. Fluid velocity and density in this case are derived as follows [31]:

$$\rho\mathbf{u}=\sum_i\mathbf{c}_i f_i+\frac{1}{2}\Delta t\cdot\mathbf{F} \tag{1.5}$$

$$\rho=\sum_i f_i. \tag{1.6}$$

The random modes $\chi_i(\mathbf{x},t)$ are fluctuating terms for the thermal noise in the fluid [18, 57]. The thermalized implementation is essentially required for the correct representation of VWF proteins and their conformations [6, 38].

1.2. Mechanical models for red blood cells and platelets

1.2.1. Bonded interactions. Each blood cell in the model is represented by a triangular mesh of Lagrangian particles (LPs) evenly spread over a cell membrane. Red blood cells (RBCs) and blood platelets differ by their sizes, shapes and mechanical properties. Therefore, for each cell a template shape was used to set the positions of corresponding LPs in the simulation box before a simulation run. Particle dynamics approach is used together with Lattice Boltzmann method and viscous fluid-structure coupling to describe the transient dynamics of the system and to obtain a cell-level hemodynamic picture. The position $\mathbf{r}$ and the velocity $\mathbf{v}$ of each LP were found from the solution of the following differential equations:

$$\frac{\mathrm{d}\mathbf{v}}{\mathrm{d}t} = \frac{(\mathbf{F}_{\text{elast}} + \mathbf{F}_{\text{int}} + \mathbf{F}_{\text{visc}})}{m}, \qquad \frac{\mathrm{d}\mathbf{r}}{\mathrm{d}t} = \mathbf{v} \tag{1.7}$$

where total force exerted on the mesh node consists of the elastic forces $\mathbf{F}_{\text{elast}}$, the non-bonded interactions $\mathbf{F}_{\text{int}}$ and the dissipative forces or viscous drag $\mathbf{F}_{\text{visc}}$.

The elastic forces account for the elasticity from stretching of edges, bending of dihedral angles between adjacent faces, as well as conservation of surface area and volume: $\mathbf{F}_{\text{elast}} = \mathbf{F}_{\text{s}} + \mathbf{F}_{\text{b}} + \mathbf{F}_{\text{a}} + \mathbf{F}_{\text{v}}$.

In the present study two versions of the material model for the blood cells are considered and compared. The 'old model' was mostly inherited (with small alterations) from the classical works [32, 19, 22, 15]. It utilizes a neo-Hookean spring law for the stretching and compression of the edges:

$$\mathbf{F}_{\text{s}} = k_{\text{s}} \Delta l \frac{\lambda^{1/2} + \lambda^{-5/2}}{\lambda + \lambda^{-3}} \mathbf{n} \tag{1.8}$$

$$\mathbf{F}_{\text{b}} = k_{\text{b}} \frac{\Delta\vartheta}{\vartheta_0} \mathbf{n}_{\text{b}} \tag{1.9}$$

$$\mathbf{F}_{\text{a}} = -k_{\text{al}} \frac{\Delta S_i}{(S_i)^{1/2}} \mathbf{w} - k_{\text{ag}} \frac{\Delta S_{\text{g}}}{S_{\text{g}}^0} \mathbf{w} \tag{1.10}$$

$$\mathbf{F}_{\text{v}} = -k_{\text{v}} \frac{\Delta V}{V_0} S_i \mathbf{n}_{\text{b}}. \tag{1.11}$$

Here k_{s} is the stretching spring constant, $\Delta l = l - l_0$ is the deviation of spring length from its equilibrium value l_0, $\lambda = l/l_0$, $\mathbf{n}$ is the unit vector pointing from one membrane point at another; k_{b} is the bending elasticity constant, $\Delta\vartheta = \vartheta - \vartheta_0$ is the deviation of dihedral angle between two adjacent triangles from ϑ_0, $\mathbf{n}_{\text{b}}$ is the unit normal vector pointing to the exterior of the cell; k_{al} and k_{ag} are the coefficients for local and global area conservation, $\Delta S_i = S_i - S_i^0$ is the change of the ith mesh triangle area, $\mathbf{w}$ is a unit vector pointing from the centroid of the triangle at the vertex; k_{v} is the coefficient of volume conservation, and $\Delta V = V - V_0$ is the cell volume change. The forces $\mathbf{F}_{\text{a}}$ and $\mathbf{F}_{\text{v}}$ are equally distributed among the vertices of ith triangle with a factor 1/3. The force $\mathbf{F}_{\text{b}}$ is applied to the vertex not belonging to the

common edge of two adjacent triangles, while the opposite force divided by two is applied to two vertices lying on the common edge.

The equilibrium lengths and angles, l_0 and ϑ_0, in this formulation are taken from the template shape of the cell, therefore the modelled RBCs have a 'memory' of their shape. On the one hand, the shape seems realistic, but on the other hand, the biconcave shape of a healthy erythrocyte physically comes from their volume depletion [49], membrane tension [41], and the physico-chemical properties of the suspending medium [51] — not from the 'pre-recorded' local curvature of the membrane. There are several published modelling works [41, 53, 13, 63], in which a variety of RBC shapes (stomatocyte-discocyte-echinocyte sequence) was obtained by minimizing the total elastic energy of the spring mesh as a result of a spheres volume decrease with a fixed surface area. The local mesh parameters l_0 and ϑ_0 are not required to be prescribed for each triangle in that case to obtain the biconcave shape of normal RBCs. Studies [41, 28, 29, 36] also show the importance of a spontaneous (yet non-local) membrane curvature arising from the area difference between the inner and outer membrane leaflets, which apprears to be an individual characteristic for each RBC.

Besides that, equation (1.8) allows for infinite stretching of the edges, while the real spectrin proteins are not infinitely extensible. While for low-to-moderate mechanical load this model gives a reasonable approximation of the RBCs dynamics, for higher forces that are typical for microvasculature and abnormal hemodynamics (stenosed arteries) it requires modifications.

The alternative version proposed in this paper (further mentioned as the 'new model') consists of the following equations:

$$\mathbf{F}_\mathrm{s} = \frac{k_\mathrm{s}\Delta l}{1-\left(\frac{\Delta l}{\Delta l_\mathrm{max}}\right)^2}\mathbf{n} \tag{1.12}$$

$$\mathbf{F}_\mathrm{b} = k_\mathrm{b}(\vartheta-\vartheta_0)\mathbf{n}_\mathrm{b} \tag{1.13}$$

$$\mathbf{F}_\mathrm{a} = -k_\mathrm{al}\frac{\Delta S_i}{(S_i^0)^{1/2}}\mathbf{w} - k_\mathrm{ag}\frac{\Delta S_\mathrm{g}}{S_\mathrm{g}^0}\mathbf{w} \tag{1.14}$$

$$\mathbf{F}_\mathrm{v} = -k_\mathrm{v}\frac{\Delta V}{V_0}S_i\mathbf{n}_\mathrm{b}. \tag{1.15}$$

Here the Finitely Extensible Nonlinear Elastic (FENE) model is used for the stretching force in (1.12), and maximal extension of the spectrin fiber was set $\Delta l_\mathrm{max} = l_0$, i.e., it can extend to twice its equilibrium length. For RBCs the resting bending angle $\vartheta_0 = \pi$ is used for all triangular elements of the mesh, so the membrane tends to flatten locally, regardless of the triangle's position in the shape template. Note that this parameter controls the spontaneous (global) curvature of the membrane and may vary for each particular cell [41]. Such formulation is more physical and, as shown below, gives a better agreement with the experiments. However, for platelets ϑ_0 is determined by the template, like in the old model, given that inactive platelets are hardly deformable and their discoid shape is maintained by the marginal tu-

Table 1. RBC material model parameterizations used in the present study. The top part of the table represents the dimensional values (marked with '*'), while the corresponding dimensionless values are at the bottom.

Parameter	M0	M1	M2	M3	M0a	Plt
k_s^* (10^{-6}N/m)	5	15	10	10	5	10^4
k_b^* (10^{-12} N)	1	2.5	2	10	1	10
k_{al}^* (10^{-16} N·m)	0	0	0	0	0.5	10
k_{ag}^* (N)	10^{-9}	10^{-9}	10^{-9}	10^{-9}	10^{-9}	10^{-9}
k_v^* (N/m^2)	10^3	10^3	10^3	10^3	10^3	10^3
k_s	0.005	0.015	0.01	0.01	0.005	10
k_b	0.001	0.0025	0.002	0.01	0.001	0.01
k_{al}	0.0	0.0	0.0	0.0	0.05	1.0
k_{ag}	1.0	1.0	1.0	1.0	1.0	1.0
k_v	1.0	1.0	1.0	1.0	1.0	1.0

bulin band of the cytoskeleton [37], which is implicit in the present coarse-grained approximation.

For each RBC the lagrangian mesh consists of 601 nodes and 1198 triangles. For platelets we use 102 nodes and 200 triangles. The parameters used in the present work are assembled in Table 1. The mass of each particle in the simulations was set to $m = 0.001$ in dimensionless units.

The circulating platelets were modelled by hardly-deformable, yet not absolutely solid, oblate spheroids. The adhesive glycoprotein Ib (GPIb) receptors of platelets were modelled as Lagrangian particles attached to the platelet membrane particles via harmonic springs, as described in [9]. GPIb receptors can specifically bind to activated VWF proteins and thus provide shear-induced platelet aggregation [42].

1.2.2. Non-bonded interactions. In addition to bonded interactions, several non-bonded conservative forces $\mathbf{F}_{\text{int}} = -\nabla U$ should be introduced. To avoid self-intersections a repulsion was added between the mesh points belonging to the same RBC in a form of truncated and shifted Lennard–Jones (LJ) interaction:

$$\mathbf{F}_{\text{self}} = -\nabla U_{\text{LJ}}^{\text{self}} \tag{1.16}$$

$$U_{\text{LJ}}^{\text{self}}(r) = 4\varepsilon_{\text{self}}\left[\left(\frac{\sigma_{\text{self}}}{r}\right)^{12} - \left(\frac{\sigma_{\text{self}}}{r}\right)^{6}\right] + U_{\text{shift}}^{\text{self}}, \quad r \leqslant r_{\text{cut}}^{\text{self}} \tag{1.17}$$

where $\sigma_{\text{self}} = r_{\text{cut}}^{\text{self}} \cdot 2^{-1/6}$ and the truncation takes place at the minimum of the potential energy. For $r > r_{\text{cut}}^{\text{self}}$ both potential and force are assumed to be zero. In the present study $r_{\text{cut}}^{\text{self}} = 0.5$. The potential was also shifted to zero at the point of truncation.

Next, it is necessary to introduce the repulsion between a cell and another cell. For this purpose, the soft-sphere interaction was used for each pair of particles be-

longing to the blood cells i and j :

$$U_{\text{rep}}^{i,j}(r) = \frac{B_{i,j}}{(r + r_{\text{off}}^{i,j})^n}, \quad r < r_{\text{cut}}^{i,j}. \tag{1.18}$$

For RBC-RBC, RBC-platelet and platelet-platelet the following values were used:

$$B_{\text{RBC,RBC}} = 0.001, \quad r_{\text{off}}^{\text{RBC,RBC}} = 0.2, \quad r_{\text{cut}}^{\text{RBC,RBC}} = 0.8 \tag{1.19}$$

$$B_{\text{RBC,plt}} = 0.002, \quad r_{\text{off}}^{\text{RBC,plt}} = 0.1, \quad r_{\text{cut}}^{\text{RBC,plt}} = 0.4 \tag{1.20}$$

$$B_{\text{plt,plt}} = 0.0001, \quad r_{\text{off}}^{\text{plt,plt}} = 0.1, \quad r_{\text{cut}}^{\text{plt,plt}} = 0.4. \tag{1.21}$$

In a similar way a short-ranged repulsion from the walls was introduced to avoid penetration:

$$B_{\text{RBC,wall}} = 0.001, \quad r_{\text{off}}^{\text{RBC,wall}} = 0.1, \quad r_{\text{cut}}^{\text{RBC,wall}} = 0.3 \tag{1.22}$$

$$B_{\text{plt,wall}} = 0.0001, \quad r_{\text{off}}^{\text{plt,wall}} = 0.2, \quad r_{\text{cut}}^{\text{plt,wall}} = 0.3. \tag{1.23}$$

The choice of these values was phenomenological. The index $n = 2$ for all presented simulations.

1.3. Model for VWF multimers

The multimers of von Willebrand factor protein were represented by a ball-and-spring free-jointed model of a linear polymer. FENE interaction was used to describe the bonds between VWF monomers:

$$F_{\text{VWF}}^{\text{bond}} = \frac{K_{\text{VWF}} \Delta r}{1 - \left(\frac{\Delta r}{\Delta r_{\max}}\right)^2} \tag{1.24}$$

where $\Delta r = r - r_0$ is the bond extension, r is the distance between neighbouring VWF beads, $r_0 = 2a$ is the equilibrium bond length, $a = 0.05\ \mu$m is the VWF subunit radius. The stiffness of the chain $K_{\text{VWF}} = 0.06\ nN/\mu$m and maximal extension of a bond $\Delta l_{\max} = 0.3\ \mu$m were obtained by fitting the experimental data from [47]. The number of monomers N in a chain was varied from 10 to 50 with the reference size of $N = 20$ corresponding to healthy VWF multimers in blood [56].

The VWF-solvent interactions were accounted as an effective attraction between VWF beads. Such an approach has proved its validity for the description of shear-dependent conformational changes of VWF [52, 6, 38, 42, 64]. The Lennard–Jones interaction (truncated at $r = 2.0 r_0$ and shifted) is used here for this purpose:

$$U_{\text{VWF}}^{LJ} = 4\varepsilon_{\text{VWF}} \left[\left(\frac{\sigma_{\text{VWF}}}{r}\right)^{12} - \left(\frac{\sigma_{\text{VWF}}}{r}\right)^{6} \right], \quad r \leqslant 2r_0, \quad \sigma_{\text{VWF}} = 2^{-1/6} r_0. \tag{1.25}$$

Soft-sphere short range repulsion (1.18) is assigned as a pair interaction between the VWF beads and the RBC particles with the index $n = 2$, the amplitude $B_{\text{VWF}} =$

0.0001, the off-set distance $r_{\text{off}}^{\text{VWF}} = a$ and the cutoff radius $r_{\text{cut}}^{\text{VWF}} = 2a$. The same soft-sphere repulsion was assigned for VWF and the vessel walls.

Finally, the adhesive interactions between VWF and platelet GPIb receptors are modelled via Morse potential:

$$U_{\text{VWF}-\text{GPIb}}(r) = A_{\text{VWF}-\text{GPIb}} \cdot \left\{ \left[1 - \mathrm{e}^{-\alpha(r-a)} \right]^2 - 1 \right\} \tag{1.26}$$

where amplitude $A_{\text{VWF}-\text{GPIb}}$ was varied in order to describe the biological variability and to investigate a possible role of mutations in cell adhesion proteins. The bond compliance parameter was chosen $\alpha = 100\mu\text{m}^{-1}$.

1.4. Coupling between the particles and the fluid

The coupling between the particles and fluid was achieved via Ahlrichs and Dunweg's point coupling method with thermal fluctuations [18, 30, 2]. According to this approach, a viscous-like force $\mathbf{F}_{\text{visc}}$ acting between the LB-fluid and a given *i*th Lagrangian particle is introduced as follows:

$$\mathbf{F}_{\text{visc}} = -\xi_i \left[\mathbf{v}_i - \mathbf{u}(\mathbf{r}, t) \right] + \mathbf{R}_i(t). \tag{1.27}$$

The first term is a Stokes-like force proportional to the difference of the particle velocity $\mathbf{v}_i$ and the local fluid velocity $\mathbf{u}$. The second term (a Langevin-like random force $\mathbf{R}(t)$) is used to resolve a thermalized behaviour of the particles, as proposed in [18] and successfully used in [57]. The opposite force $-\mathbf{F}_{\text{visc}}$ is transferred back to the fluid.

The parameter of friction ξ_i should be defined individually for each particle type in order to reproduce the correct behaviour observed species in experiments. In present implementation an individual friction coefficient is used for each particle, providing a possibility for correct and precise tuning of drag forces on platelets, RBCs and VWF in our coarse-grained simulations. For platelets and VWFs the friction coefficients ξ_{plt} and ξ_{VWF} were tuned and validated in previous studies [7, 38]. These coefficients depend on the dynamic viscosity μ of the fluid. For the physiological value of blood plasma viscosity ($\mu \approx 1.5$ mPa·s) the appropriate extimation is $\xi_{\text{plt}} = 0.23 \cdot 10^{-9}$ N·s/m and $\xi_{\text{VWF}} = 1.5/58 \cdot 10^{-8} \approx 0.25862 \cdot 10^{-9}$ N·s/m. These values are scaled linearly with μ in present model. Precise tuning of ξ_{VWF} is based on experimental data from [27]. The situation is a bit more complicated for RBCs, as described further in text.

2. Results

2.1. Tweezing of RBC: validation of new material model

In order to adjust the parameters and validate the biomechanical model of RBCs the initial set of simulations was devoted to a single erythrocyte in different mechanical conditions. Firstly, it is necessary to make sure that the elasticity of the model RBCs

is realistic. The single cell optical tweezers experiments[45] that are nowadays treated as a 'gold standard' in validation of erythrocyte biomechanics were used as a benchmark. For this case there is no net flow of the fluid, the modelled cell is fixed in space by a spot on its rim and pulled apart by a constant force applied to another spot in the opposite side of the rim (equally distributed among the nodes within the contact area). This imitates the actual experiment when the cell is attached to a pair of spherical beads via a finite contact area. The elongation of the cell in axial and transversal directions is measured when the deformation reaches the steady state. Since the elongation of the cell depends on the contact spot size, the diameter of the contact area in the model was 2 μm — the same as in [45]. There were several parameterizations used for this stage of validation (see Table 1) and the results for two material models described above were compared with the experiments. The results presented in Fig. 2 suggest that the new material model better describes the experimentally measured elasticity of RBCs for intermediate and high forces. The most appropriate parameterization corresponds to the model M0.

2.2. RBC in shear: high plasma viscosity

After validating the elastic properties of the RBC in the model, the coupling coefficient ξ_{RBC} should be appropriately chosen, according to a different kind of experiments. We need to establish to what extent the flow of a viscous fluid can deform the cell. Several experiments on the dynamics of individual RBCs in a plane shear flow are known from the literature [25, 62, 20]. It is well known that a transition occurs from a tumbling/rolling (TR) of a rigid discocyte RBC at low shear rates to a fluidized tank-treading (TT) motion of RBC membrane at higher shear rates. This characteristic TT regime was also observed in the simulations (see Fig. 3), thus indicating qualitative agreement between the model and real cell dynamics.

The paper by Tran-Son-Tay et al. [62] reports longitudinal and transversal sizes of RBCs performing TT motion under different shear rates. These results are suitable for tuning ξ_{RBC} in the present model. However, most of the available experiments were conducted in a fluid of non-physiological high viscosity, e.g., 58 cP in [62]. Thus for the first set of data fitting the viscosity of the fluid in the model was increased. Figure 4 illustrates the results of both old and new models, and compares the calculations with real RBCs. This study shows that again the new model gives a better fit of experiments. Appropriate value of the friction parameter ξ_{RBC} should be chosen from a range 0.1–0.2 in dimensionless units, which corresponds to 10^{-8}–$2 \cdot 10^{-8}$ N·s/m. The upper value, however, is better in terms of cell deformation.

2.3. RBC in shear: low plasma viscosity

More recent experiments by Yao et al. [67] were performed in a low-viscosity medium. The authors observed erythrocytes rolling in a shear flow of a buffer with $\mu = 0.707$ cP and calculated the deformation index by processing the photographs.Interestingly, they observed that rigid rolling RBCs orient themselves in

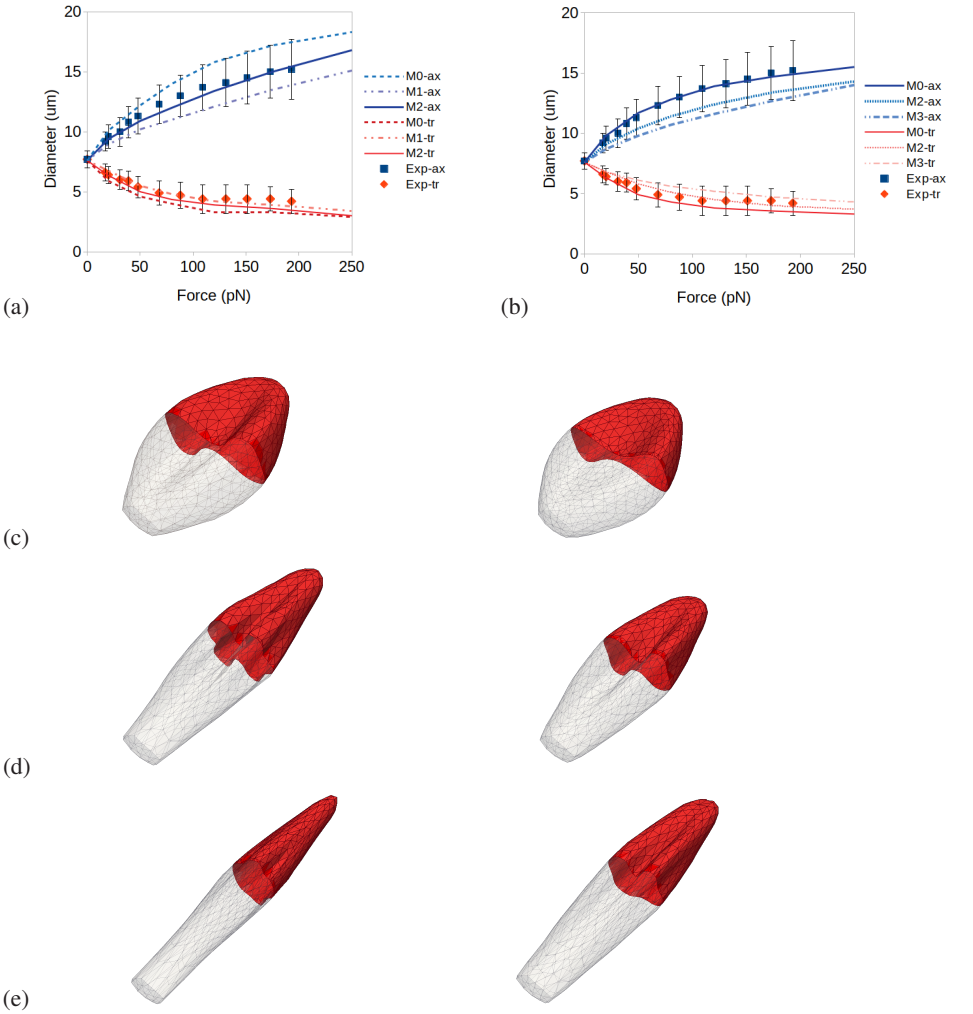

Figure 2. Deformations of RBCs under uniaxial force-clamp tweezing for old (a) and new (b) material models. Blue lines indicate the RBC size along the force (axial direction), and the red ones — in transversal direction. Different parameterizations correspond to different linestyles. The symbols (blue squares and red diamonds) indicate the experimental data from [45]. Panels (c-e) visualize the RBC shapes (old model — left, new — right) under load: (c) 20 pN, (d) 80 pN, (e) 250 pN.

the plane of shear, since tumbling motion of oblate rigid particles is unstable [17].

The results from the simulations are found to be in a reasonable agreement with these experiments (see Fig. 5), if the friction coefficient $\xi_{\mathrm{RBC}} = 0.7/35.0 \cdot 10^{-8}$ $\mathrm{N \cdot s/m} = 0.02 \cdot 10^{-8}$ $\mathrm{N \cdot s/m}$. In other words, if one applies the linear scaling $\xi_{\mathrm{RBC}} \propto \mu$ then the estimation from previous subsection seems correct:

$$\xi_{\mathrm{RBC}} = \frac{\mu[\mathrm{cP}]}{35} \cdot 10^{-8} \mathrm{N \cdot s/m} \tag{2.1}$$

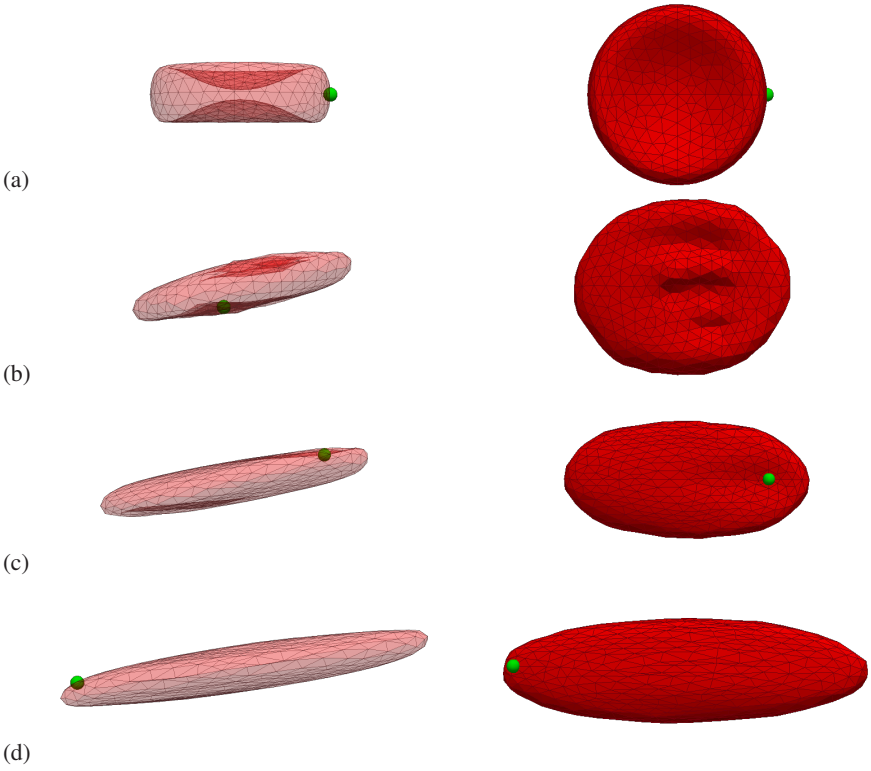

Figure 3. Simulated steady tank-treading (TT) motion of an RBC (new model, M0) in sheared fluid with $\mu = 35$ cP at different shear rates: (a) 0, (b) 20, (c) 75, (d) 150 s^{-1}. The green marker was used to track the membrane motion and measure the TT frequency.

where $\mu[\mathrm{cP}]$ is the dynamic viscosity of the surrounding medium expressed in centipoise units (1 cP = 1 mPa · s). However, to achieve a more realistic RBC deformation at high viscosity, one may consider an alternative fitting formula that gives a nonlinear (quadric) approximation:

$$\xi_{\mathrm{RBC}} = (0.000833 \cdot \mu[\mathrm{cP}]^2 + 0.027988 \cdot \mu[\mathrm{cP}]) \cdot 10^{-8} \mathrm{N} \cdot \mathrm{s/m}. \qquad (2.2)$$

For blood plasma at physiological conditions $\mu \approx 1.5$ cP, therefore, both formulas give $\xi_{\mathrm{RBC}} \approx 0.03 \cdot 10^{-8}$ N · s/m, which was used in all further simulations.

A series of simulations of an individual RBC in a plane shear flow has been performed for different values of ξ_{RBC} and different shear rates (see Fig. 6), while the kinematic viscosity of the fluid ν was kept constant. Indeed, except the tumbling/rolling (TR) of non-deformed discocytes and the tank-treading (TT) of fluidized cells, a spectrum of transient modes of deformed (D) erythrocyte movement was observed in the simulation.

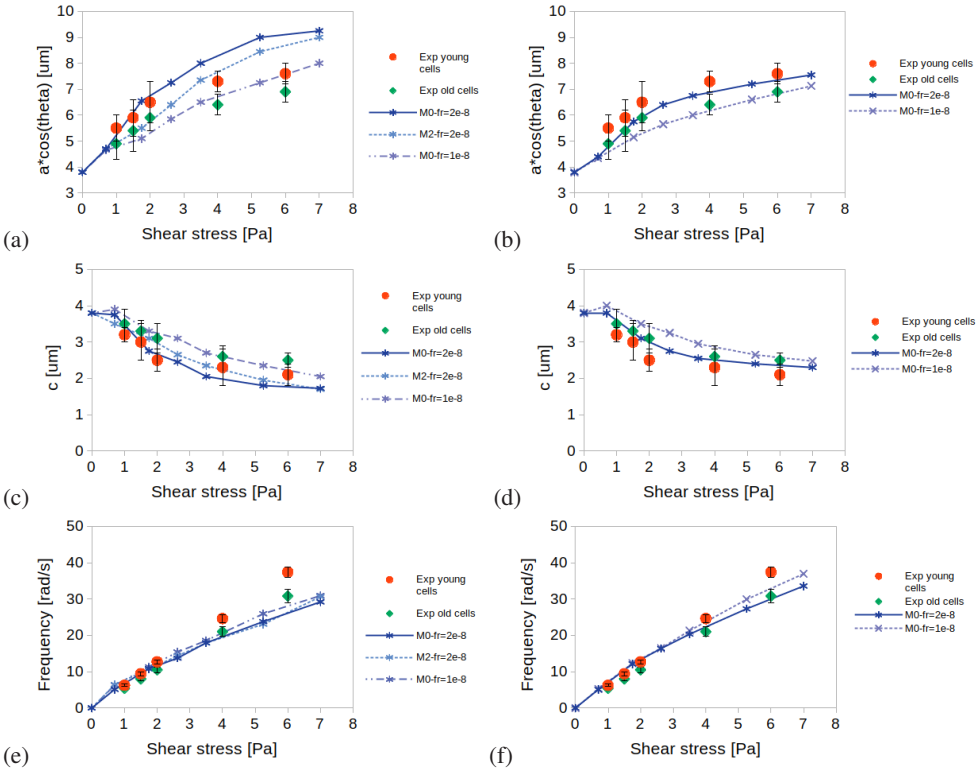

Figure 4. RBC deformations and dynamics during tank-treading in sheared fluid with $\mu = 35$ cP for old (a,c,e) and new (b,d,f) material models. (a,b) Projected RBC length vs. shear stress. (c,d) RBC width vs. shear stress. (e,f) Frequency of the tank-treading. Symbols with lines correspond to simulations, red circles and green diamonds indicate the experimental data from [62]. In panels (a,c,e): solid line is for M0, $\xi_{\mathrm{RBC}} = 2 \cdot 10^{-8}$ N·s/m; dashed line is for M2, $\xi_{\mathrm{RBC}} = 2 \cdot 10^{-8}$ N·s/m; dash-dotted line is for M0, $\xi_{\mathrm{RBC}} = 1 \cdot 10^{-8}$ N·s/m. In panels (b,d,f): solid line is for M0, $\xi_{\mathrm{RBC}} = 2 \cdot 10^{-8}$ N·s/m; dashed line is for M0, $\xi_{\mathrm{RBC}} = 1 \cdot 10^{-8}$ N·s/m.

2.4. Shapes of an individual RBC in a shear flow

Recent experiments of Lanotte et al. [40] showed an interesting result: except rolling or tumbling of discocytes and TT motion, RBCs can attain a variety of deformed intermediate shapes (stomatocytes, trilobes and multilobes) under low viscosity and physiologically relevant shear rates. In order to further validate the dynamics of RBCs in the present model, let us qualitatively compare the RBC shapes in our simulations and these experiments [40].

In conditions that are close to physiological, namely for $\mu = 1$ cP, a series of RBC motion regimes is observed in the simulations (see Fig. 7). For low shear the cell maintains the discocyte shape and performs tumbling (see Fig. 7a), or rolling (see Fig. 5c). As the shear rate increases, the cell keeps tumbling as a stomatocyte (see Fig. 7(b,c)). Then the stomatocyte deforms even more, this deformation leads to several multilibe shapes (see Fig. 7d), that have been observed experimentally

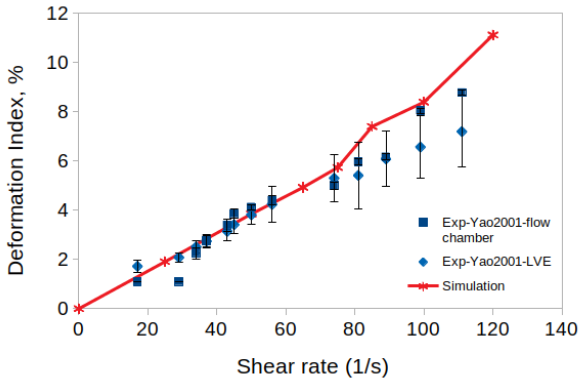

(a)

(b) (c)

Figure 5. (a) Deformation index of RBC during its rolling in a sheared fluid with $\mu = 0.7$ cP: line with symbols corresponds to simulations, while squares and diamonds correspond to measurements from [67]. Simulated RBC in steady (b) and sheared (c) fluid (shear is imposed in the plane of the picture). The deformation index is calculated as $100\% \cdot (a-b)/(a+b)$, where a and b are lengths of the major and minor half-axes of the RBC.

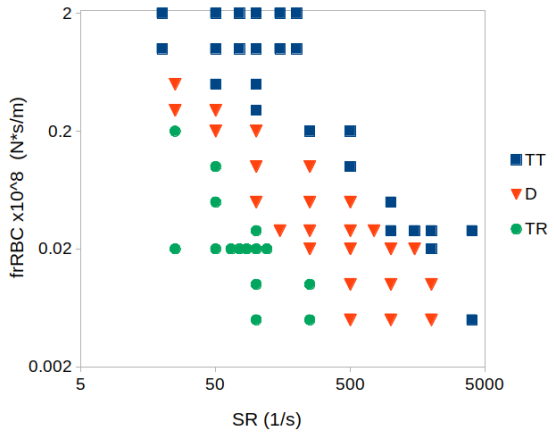

Figure 6. Diagram of the RBC motion regimes for different friction coefficients ξ_{RBC} (vertical axis) and various shear rates (horizontal axis). The squares correspond to the tank-treading (TT) motion, the circles correspond to non-deformed tumbling or rolling, and the triangles correspond to a variety of deformed shapes.

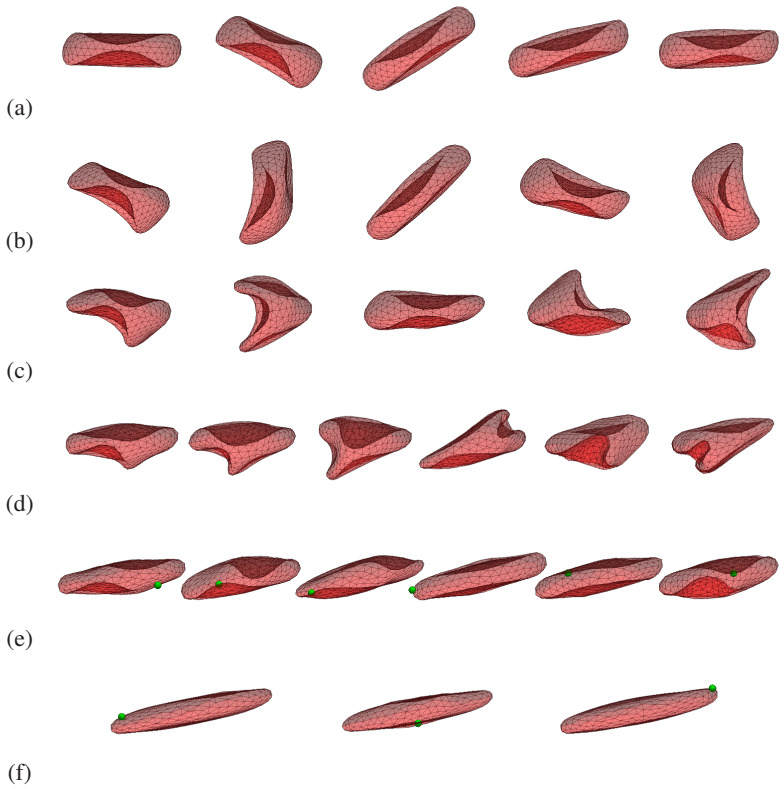

Figure 7. Different regimes of RBC motion in a shear flow of viscous fluid ($\mu = 1$ cP) at different shear rates: (a) tumbling discocyte at 100 s^{-1}; (b) tumbling stomatocyte at 150 s^{-1} ; (c) tumbling deformed stomatocyte at 250 s^{-1}; (d) multilobe (trilobe) shape at 500 s^{-1}; (e) breathing (vacillating) tank-treading at 1000 s^{-1}; (f) steady tank treading at 4000 s^{-1}. The cells are clipped at the cross-section and made transparent for visibility.

in [40]. Further increase of the shear rate forces the RBC to stretch, suppresses the lobes and protrusions, and leads to a breathing tank-treading (BTT) regime (see Fig. 7e), which is finally replaced by a steady TT motion at extremely high shear rates (see Fig. 7f). These results agree with [40, 43].

Next, the outer medium viscosity was varied in the simulations and the aforementioned scaling of outer medium viscosity μ was applied (see Fig. 8). Also in this figure various experimentally observed shapes are denoted for comparison, according to [25, 62, 20, 40, 67]. Finally, the effect of local area conservation on RBC shapes and dynamical regimes was investigated via simulations (see Fig. 9). Increase of the parameter k_{al} expands the detection range of multilobed and deformed shapes, and moves the onset of TT regime to higher shear rates.

Overall, the simulations are in a reasonable qualitative agreement with the experiments. Several descrepancies exist, however, they can be attributed to the natural variability of blood cells and the inevitable consequences from coarse-graining of

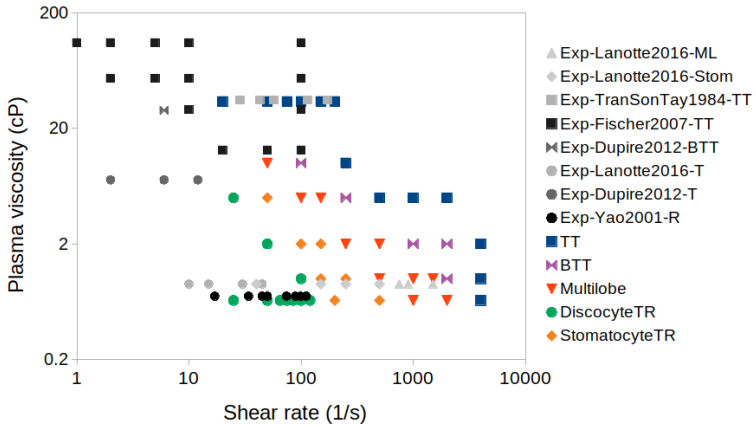

Figure 8. State diagram for RBC shapes under shear flow. Each point corresponds to a certain shear rate (horizontal axis) and a certain value of the dynamic viscosity of the surrounding medium (blood plasma). Coloured symbols correspond to the simulations, while the experimental observations from [25, 62, 20, 40, 67] are in the shades of grey. The legend notation is as follows: TT—tank-treading, BTT—breathing tank-treading, ML—multilobes, TR— tumbling or rolling, R—rolling, Stom—stomatocyte.

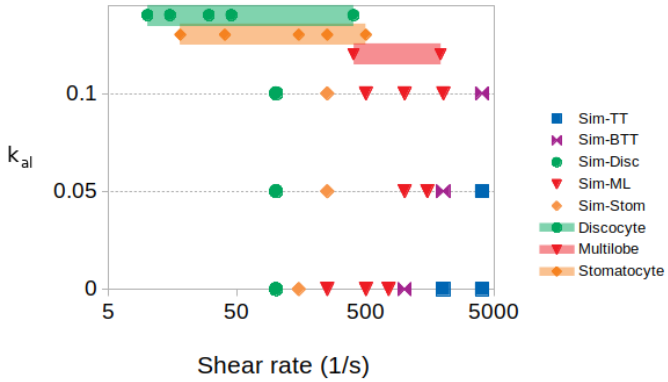

Figure 9. Diagram illustrating the effect of local area conservation parameter k_{al} on motion regime of RBC under shear ($\mu = 1$ cP). The symbols correspond to different RBC shapes in the simulations: tank-treading (Sim-TT), breathing tank-treading (Sim-BTT), discocyte (Sim-Disc), multilobe (Sim-ML), stomatocyte (Sim-Stom). The coloured bars on top indicate the experimentally observed ranges for discocytes (green), stomatocytes (orange) and multilobes (red) in the whole blood experiments[40].

the model. Based on these results, the model for RBC was found to be validated, and further simulation of dense suspensions should be trustworthy.

2.5. Simulations of dense RBC-platelet suspension flow in a microtube

For illustration of the applicability of the presented model, let us describe here the simulation result obtained for pressure-driven flow of a dense suspension of RBCs and platelets in a microvessel. Simulations performed in an arteriole with a diameter of 32 μm for a typical Reynolds number $\mathrm{Re} = 0.05$ are presented in Fig. 10. All

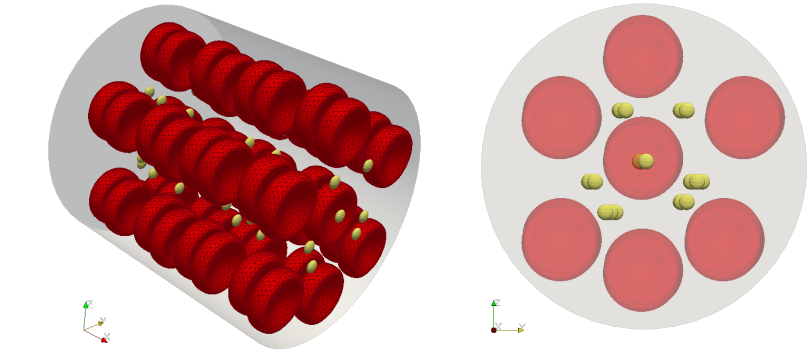

(a)

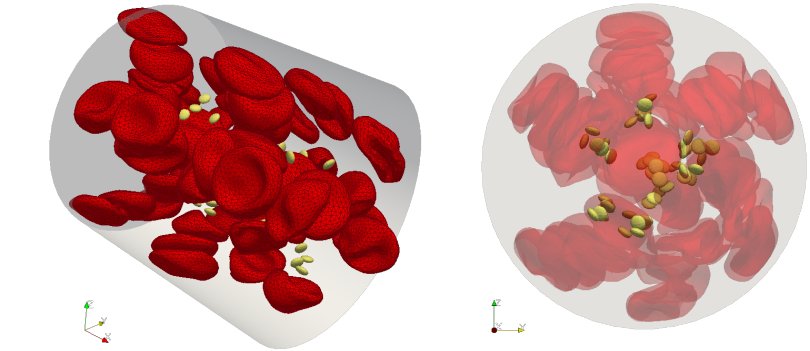

(b)

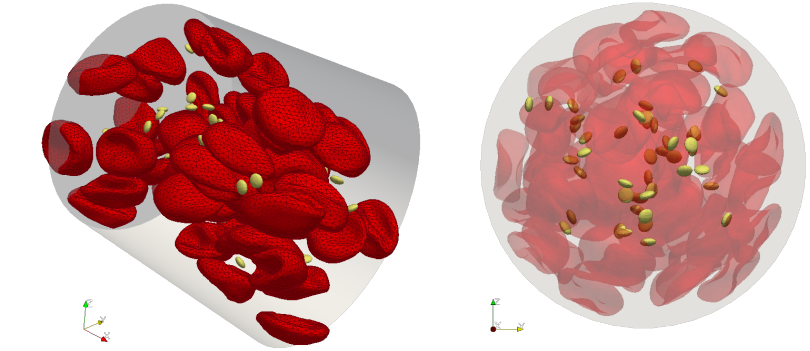

(c)

Figure 10. Simulations of RBC-platelet suspension in a microvessel (arteriole with a diameter of 32 μm) at Re $= 0.05$ (wall shear rate $\dot{\gamma} \approx 450$ s^{-1}) at different moments of time: (a) 0, (b) 100, (c) 499 ms.

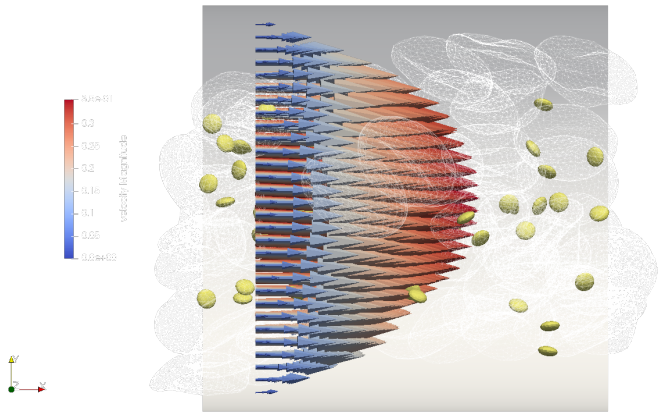

Figure 11. Flow velocity profile for simulations with Re = 0.05.

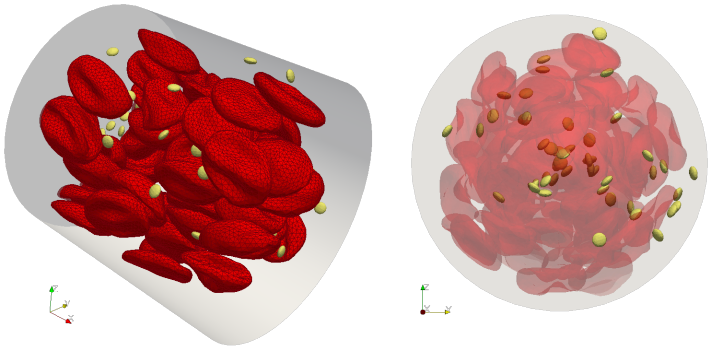

(a)

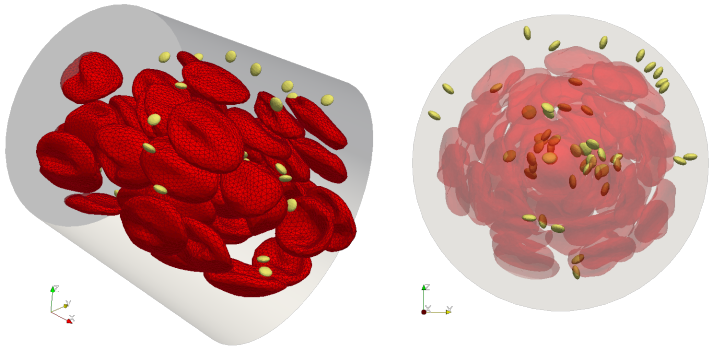

(b)

Figure 12. Simulations of blood flow in the 32 μm-arteriole with different Reynolds numbers after 500 milliseconds: (a) Re = 0.1 (wall shear rate $\dot{\gamma} \approx 968$ s^{-1}), (b) Re = 0.2 (wall shear rate $\dot{\gamma} \approx 2064$ s^{-1}).

simulations are performed with the new model (M0a). Blood plasma viscosity was 1.5 cP. Initial placement of the cells was in a form of regular stacks, as presented in Fig. 10a. The platelets were placed far from the walls. It is instructive to study the near-wall depleted layer formation and platelet margination dynamics. After 100 ms the regular pattern was broken and the configuration of cells aquired a tendency to chaotisation, Fig. 10b. One can see that by the end of the simulation run (499 ms) (see Fig. 10c), not all platelets are expelled to the periphery of the vessel. The flow velocity profile was parabolic, as expected (see Fig. 11). The average wall shear rate calculated from this profile is $\dot{\gamma} \approx 450\ \mathrm{s}^{-1}$.

Simulations at higher Reynolds numbers revealed that the formation of the cell-free layer is promoted by higher shear rates near the vessel walls, as illustrated in Fig. 12. Here the initial state was identical to Fig. 10a. For $\mathrm{Re} = 0.1$ a cell-free layer reaches 1–1.5 μm and some amount of platelets are expelled to the periphery, yet still experience collisions with RBCs and perform irregular tumbling-like motion (see Fig. 12a). For $\mathrm{Re} = 0.2$ the cell-free layer becomes much more noticeable (see Fig. 12b), and the marginated platelets have enough space to move without collisions with RBCs. One can notice that near-wall platelets in simulations tend to rolling under these hemodynamic conditions.

2.6. Simulations of platelet adhesion to inflamed microvessel walls

Finally, let us inspect the biomechanics of platelet adhesion to von Willebrand factor by means of computer simulations. In order to achieve the platelet margination in a shorter simulation time, a smaller blood vessel (12 μm capillary) is considered in this example. The Reynolds number was set to $\mathrm{Re} = 0.02$ in order to reach the wall shear rate $\dot{\gamma} \approx 2000\,\mathrm{s}^{-1}$ that is typical for arterioles, where platelet hemostasis is essential. The amount of 100 VWF multimers were attached to the vessel walls in order to simulate inflammataion and secretion of VWF by the endothelium. In addition, another set of 100 VWF were freely suspended in the bulk fluid. All VWF multimers consisted of 20 subunits. The intermonomer attraction parameter was set to $\varepsilon_{\mathrm{VWF}} = 4\ k_{\mathrm{B}}T$, the adhesion energy $A_{\mathrm{VWF-GPIb}} = 50\ k_{\mathrm{B}}T$.

The results presented in Fig. 13 suggest that the wall-grafted VWFs are elongated and activated by the shear flow, while the free flowing multimers maintain the collapsed shape. The marginated platelets adhere to the wall-grafted VWFs in a small amount, not causing the thrombotic conditions during the simulated timespan. In future it would be instructive to perform series of simulations for various parameters of platelet-VWF interaction.

3. Discussion and conclusion

In this paper a three-dimensional hemodynamic model for cell-resolving simulations was presented. Much attention in this work is paid to the development of a more accurate biomechanical model of the erythrocyte for use in models of cellular hemostasis. A modification of the known models was proposed to accurately take into account the elastic properties of the erythrocytes. The new model showed bet-

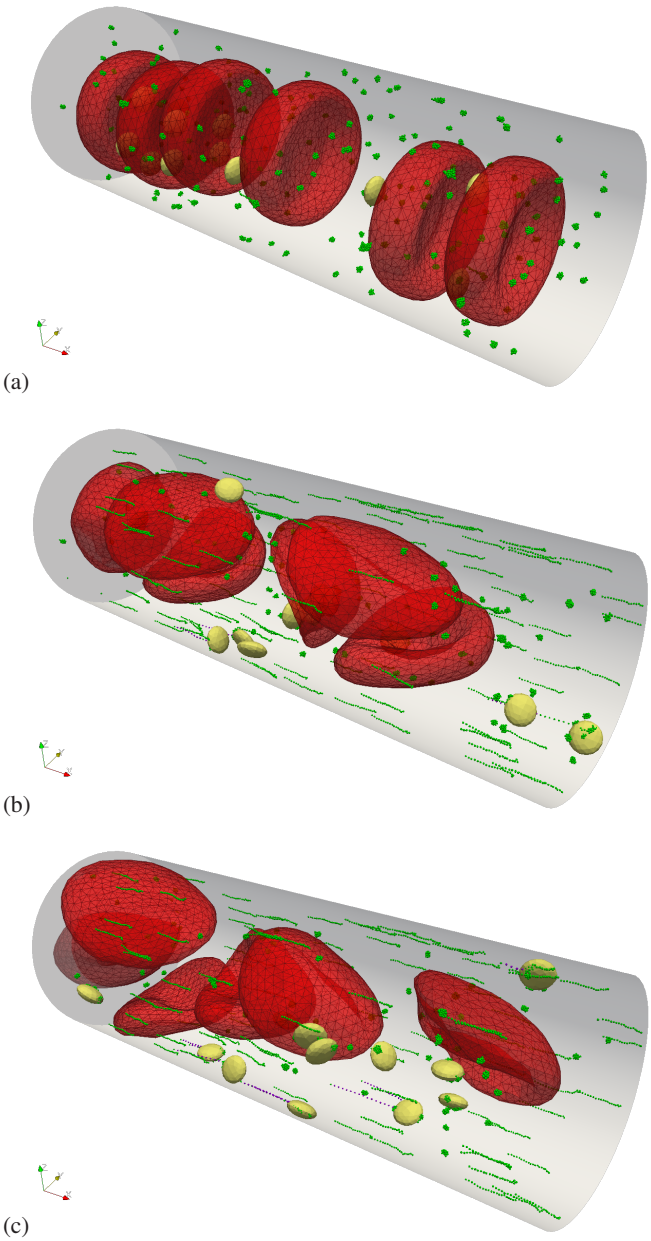

(a)

(b)

(c)

Figure 13. Simulation of whole blood flow in an inflamed microvessel (12 μm in diameter) with 100 VWF multimers (20 subunits each) exposed by the endothelium (attached to the walls) in presence of the free flowing VWFs in plasma at different time moments: (a) $t = 0$, (b) $t = 50$, (c) $t = 130$ ms. The purple beads indicate the overstretched (>20 pN) and thus activated VWF monomers that are capable of stronger platelet adhesion [27, 9]. The Reynolds number Re $= 0.02$, the wall shear rate $\dot{\gamma} \approx 2000$ s^{-1}.

ter agreement with the experimental results. The parameters were selected from a comparison of the dynamics of the model system with different experiments from the literature. The proposed model is not the only possible one. Several alternative variants and implementations are well known [68, 43, 22, 16]. For instance, in [35] the non-uniform force distribution for the local area conservation is proposed, which is useful for simulations of cells in cramped conditions.

Another issue raised in the present paper concerns the exact selection of viscous friction coefficients for each of the system objects. This paper shows that, using independent experiments published in the literature to date, it seems possible to tune the system accurately enough to reproduce the hemodynamic effects, at least phenomenologically.

The model is capable of efficient simulations of the whole blood flow in realistic hydrodynamic conditions, high hematocrit, and arteriole- or venule-sized blood vessels. The simulations qualitatively reproduce the Fahraeus–Lindquist effect and consequent platelet margination. VWF-dependent platelet aggregation can also be simulated using this framework. Further studies may be devoted to the investigation of the RBC aggregation effects in microvasculature. Another possible way for modification is more accurate accounting of the mechanical properties of the spectrin network and cell membrane via molecular modelling.

Currently, increasing attention is paid to explicit modelling of platelet adhesion to von Willebrand factor multimers, as it may shed light on various hemostatic disorders and pathological conditions. Since the first publications on shear-induced conformation changes of VWF [52, 4] this topic has attracted researchers from different non-medical areas, including polymer physics, computational physics and hydrodynamics. Several works (see, e.g., [50, 34, 33]) addressed the primary hemostasis via classical dissipative particle dynamics modelling, and described margination, stretching and size regulation of VWFs. In [7, 6, 38] an alternative numerical approach, a combination of PD and LBM, was tested and used to quantify the effect of VWF size on initial platelet hemostasis. The possibility of platelet mechanical activation during adhesion to surface-immobilized VWF was also investigated in [9]. Recent experiments [11] and improved higher-resolution models [39, 8] should help to obtain a more accurate biophysical picture of VWF mechanochemistry that could be used in hemodynamic simulations and biomedical applications. Another remarkable recent study [42] reproduced the shear-induced platelet aggregation at high shear rates in silico by simulating soluble VWF and nonactivated platelets (adopting a spherical shape) in blood plasma without RBCs via a similar LBM-Langevin dynamics approach. The effect of platelet shape and size, as well as their cytoskeleton restructuring under shear might be an intriguing direction to study in future using numerical simulations.

Acknowledgement: The research was carried out using the equipment (supercomputer Lomonosov-2) of the shared research facilities of HPC computing resources at Lomonosov Moscow State University [66].

References

1. R. Adhikari, K. Stratford, M. E. Cates, and A. J. Wagner, Fluctuating lattice Boltzmann. *Europhysics Letters (EPL)* **71** (2005), 473–479.
2. P. Ahlrichs and B. Dunweg, Simulation of a single polymer chain in solution by combining lattice Boltzmann and molecular dynamics. *The Journal of Chemical Physics* **111** (1999), 8225–8239.
3. A. Albanese, L. Cheng, M. Ursino, and N. W. Chbat, An integrated mathematical model of the human cardiopulmonary system: model development. *American Journal of Physiology-Heart and Circulatory Physiology* **310** (2016), H899–H921.
4. A. Alexander-Katz and R. R. Netz, Surface-enhanced unfolding of collapsed polymers in shear flow. *Europhysics Letters* **80** (2007), 18001.
5. A. V. Belyaev, M. A. Panteleev, and F. I. Ataullakhanov, Threshold of microvascular occlusion: injury size defines the thrombosis scenario. *Biophysical Journal* **109** (2015), 450–456.
6. A. V. Belyaev, Catching platelets from the bloodflow: the role of the conformation of von Willebrand factor. *Mat. Mod. Nat. Phenom.* **13** (2018), 44.
7. A. V. Belyaev, Long ligands reinforce biological adhesion under shear flow. *Phys. Rev. E* **97** (2018), 042407.
8. A. V. Belyaev, Intradimer forces and their implication for conformations of von Willebrand factor multimers. *Biophysical Journal* **120** (2021), 899–911.
9. A. V. Belyaev and Y. K. Kushchenko, Biomechanical activation of blood platelets via adhesion to von Willebrand factor studied with mesoscopic simulations. *Biomechanics and Modeling in Mechanobiology* **22** (2023), 785–808.
10. A. V. Belyaev, J. L. Dunster, J. M. Gibbins, M. A. Panteleev, and V. Volpert, Modelling thrombosis in silico: frontiers, challenges, unresolved problems and milestones. *Physics of Life Reviews* **26-27** (2018), 57–95.
11. H. T. Bergal, Y. Jiang, D. Yang, T. A. Springer, and W. P. Wong, Conformation of von Willebrand factor in shear flow revealed with stroboscopic single-molecule imaging. *Blood* **140** (2022), 2490–2499.
12. N. Bessonov, E. Babushkina, S. F. Golovashchenko, A. Tosenberger, F. Ataullakhanov, M. Panteleev, A. Tokarev, and V. Volpert, Numerical modelling of cell distribution in blood flow. *Math. Model. Nat. Phenom.* **9** (2014), 69–84.
13. M. Chen and F. J. Boyle, An enhanced spring-particle model for red blood cell structural mechanics: application to the stomatocyte-discocyte-echinocyte transformation. *Journal of Biomechanical Engineering* **139** (2017).
14. S. Chen and G. D. Doolen, Lattice Boltzmann method for fluid flows. *Annual Review of Fluid Mechanics* **30** (1998), 329–364.
15. I. Cimrák, M. Gusenbauer, and I. Jančigová, An ESPResSo implementation of elastic objects immersed in a fluid. *Computer Physics Communications* **185** (2014), 900–907.
16. I. Cimrák, M. Gusenbauer, and T. Schrefl, Modelling and simulation of processes in microfluidic devices for biomedical applications, *Computers and Mathematics with Applications* **64** (2012), 278–288, Mathematical Methods and Models in Biosciences.
17. Z. Cui, L. Zhao, W.-X. Huang, and C.-X. Xu, Stability analysis of rotational dynamics of ellipsoids in simple shear flow. *Physics of Fluids* **31** (2019), No. 2.
18. B. Dunweg and A. J. C. Ladd, *Lattice Boltzmann Simulations of Soft Matter Systems*, Adv. in Polymer Sci., Springer, Berlin–Heidelberg, 2008, pp. 1–78.
19. M. M. Dupin, I. Halliday, C. M. Care, L. Alboul, and L. L. Munn, Modeling the flow of dense

suspensions of deformable particles in three dimensions. *Phys. Rev. E.* **75** (2007), 066707.

20. J. Dupire, M. Socol, and A. Viallat, Full dynamics of a red blood cell in shear flow. In: *Proceedings of the National Academy of Sciences* **109** (2012), 20808–20813.

21. R. Fahraeus and T. Lindqvist, The viscosity of the blood in narrow capillary tubes. *American Journal of Physiology-Legacy Content* **96** (1931), 562–568.

22. D. A. Fedosov, M. Dao, G. E. Karniadakis, and S. Suresh, Computational bio-rheology of human blood flow in health and disease. *Ann. Biomed. Eng.* **42** (2014), 368–387.

23. D. A. Fedosov and G. E. Karniadakis, Triple-decker: interfacing atomistic-mesoscopic-continuum flow regimes. *J. Comput. Phys.* **228** (2009), 1157–1171.

24. D. A. Fedosov, B. Caswell, A. S. Popel, and G. E. Karniadakis, Blood flow and cell-free layer in microvessels: blood flow and cell-free layer in microvessels. *Microcirculation* **17** (2010), 615–628.

25. T. M. Fischer, Tank-tread frequency of the red cell membrane: dependence on the viscosity of the suspending medium. *Biophysical Journal* **93** (2007), 2553–2561.

26. A. L. Fogelson and N. Tania, Coagulation under flow: the influence of flow-mediated transport on the initiation and inhibition of coagulation. *Pathophysiology of Haemostasis and Thrombosis* **34** (2005), 91–108.

27. H. Fu, Y. Jiang, D. Yang, F. Scheiflinger, W. P. Wong, and T. A. Springer, Flow-induced elongation of von Willebrand factor precedes tension-dependent activation. *Nature Communications* **8** (2017), 324.

28. N. M. Geekiyanage, M. A. Balanant, E. Sauret, S. Saha, R. Flower, C. T. Lim, and Y.-T. Gu, A coarse-grained red blood cell membrane model to study stomatocyte-discocyte-echinocyte morphologies. *PLOS ONE* **14** (2019), e0215447.

29. N. M. Geekiyanage, R. Flower, Y. T. Gu, and E. Sauret, *An Improved Coarse-Grained Model to Accurately Predict Red Blood Cell Morphology and Deformability*. Springer International Publishing, 2020, pp. 47–84.

30. G. Giupponi, G. De Fabritiis, and P. V. Coveney, Hybrid method coupling fluctuating hydrodynamics and molecular dynamics for the simulation of macromolecules. *The Journal of Chemical Physics* **126** (2007), 154903.

31. Z. Guo, C. Zheng, and B. Shi, Discrete lattice effects on the forcing term in the lattice Boltzmann method. *Physical Review E* **65** (2002), No. 4, 046308.

32. J. C. Hansen, R. Skalak, S. Chien, and A. Hoger, An elastic network model dased on the structure of the red blood cell membrane skeleton. *Biophysical Journal* **70** (1996), 146–166.

33. M. Hoore, K. Rack, D. A. Fedosov, and G. Gompper, Flow-induced adhesion of shear-activated polymers to a substrate. *Journal of Physics: Condensed Matter* **30** (2018), 064001.

34. B. Huisman, M. Hoore, G. Gompper, and D. A. Fedosov, Modeling the cleavage of von Willebrand factor by ADAMTS13 protease in shear flow, *Medical Engineering & Physics* **48** (2017), 14–22.

35. I. Jancigova and I. Cimrak, Non-uniform force allocation for area preservation in spring network models. *International Journal for Numerical Methods in Biomedical Engineering* **32** (2015).

36. D. M. W. Karandeniya, D. W. Holmes, E. Sauret, and Y. T. Gu, A new membrane formulation for modelling the flow of stomatocyte, discocyte, and echinocyte red blood cells. *Biomechanics and Modeling in Mechanobiology* **21** (2022), 899–917.

37. Q. Kimmerlin, S. Moog, A. Yakusheva, C. Ziessel, A. Eckly, M. Freund, G. Zvodszky, Y. Knapp, P. Mangin, and F. Lanza, Loss of α4A- and β1-tubulins leads to severe platelet spherocytosis and strongly impairs hemostasis in mice. *Blood* **140** (2022), 2290–2299.

38. Y. K. Kushchenko and A. V. Belyaev, Effects of hydrophobicity, tethering and size on flow-induced activation of von Willebrand factor multimers. *Journal of Theoretical Biology* **485** (2020), 110050.

39. O. Languin-Catton, E. Laborie, D. O. Yurkova, S. Melchionna, P. Derreumaux, A. V. Belyaev, and F. Sterpone, Exposure of von Willebrand factor cleavage site in A1A2A3-fragment under extreme hydrodynamic shear. *Polymers* **13** (2021), 3912.

40. L. Lanotte, J. Mauer, S. Mendez, D. A. Fedosov, J.-M. Fromental, V. Claveria, F. Nicoud, G. Gompper, and M. Abkarian, Red cells' dynamic morphologies govern blood shear thinning under microcirculatory flow conditions. *Proceedings of the National Academy of Sciences* **113** (2016), 13289–13294.

41. G. H. W. Lim, M. Wortis, and R. Mukhopadhyay, Stomatocyte-discocyte-echinocyte sequence of the human red blood cell: Evidence for the bilayer-couple hypothesis from membrane mechanics, *Proceedings of the National Academy of Sciences* **99** (2002), 16766–16769.

42. Z. L. Liu, C. Bresette, C. K. Aidun, and D. N. Ku, SIPA in 10 milliseconds: VWF tentacles agglomerate and capture platelets under high shear. *Blood Advances* **6** (2022), 2453–2465.

43. J. Mauer, S. Mendez, L. Lanotte, F. Nicoud, M. Abkarian, G. Gompper, and D. A. Fedosov, Flow-induced transitions of red blood cell shapes under shear. *Physical Review Letters* **121** (2018), No. 11, 118103.

44. M. J. Maxwell, E. Westein, W. S. Nesbitt, S. Giuliano, S. M. Dopheide, and S. P. Jackson, Identification of a 2-stage platelet aggregation process mediating shear-dependent thrombus formation. *Blood* **109** (2007), 566–576.

45. J. P. Mills, L. Qie, M. Dao, C. T. Lim, and S. Suresh, Nonlinear elastic and viscoelastic deformation of the human red blood cell with optical tweezers. *Mol. Cell. Biomech.* **1** (2004), 169.

46. L. Mountrakis, E. Lorenz, and A. G. Hoekstra, Where do the platelets go? A simulation study of fully resolved blood flow through aneurysmal vessels. *Interface Focus* **3** (2013), 20120089.

47. J. P. Müller, S. Mielke, A. Löf, T. Obser, C. Beer, L. K. Bruetzel, D. A. Pippig, W. Vanderlinden, J. Lipfert, R. Schneppenheim, and M. Benoit, Force sensing by the vascular protein von Willebrand factor is tuned by a strong intermonomer interaction. *Proceedings of the National Academy of Sciences* **113** (2016), 1208–1213.

48. J. M. O'Sullivan, D. McGonagle, S. E. Ward, R. J. S. Preston, and J. S. O'Donnell, Endothelial cells orchestrate COVID-19 coagulopathy. *The Lancet Haematology* **7** (2020), e553–e555.

49. Z. Peng, A. Mashayekh, and Q. Zhu, Erythrocyte responses in low-shear-rate flows: effects of non-biconcave stress-free state in the cytoskeleton. *Journal of Fluid Mechanics* **742** (2014), 96–118.

50. K. Rack, V. Huck, M. Hoore, D. Fedosov, S. Schneider, and G. Gompper, Margination and stretching of von Willebrand factor in the blood stream enable adhesion. *Scientific Reports* **7** (2017), 14278.

51. W. H. Reinhart, N. Z. Piety, J. S. Goede, and S. S. Shevkoplyas, Effect of osmolality on erythrocyte rheology and perfusion of an artificial microvascular network. *Microvascular Research* **98** (2015), 102–107.

52. S. W. Schneider, S. Nuschele, A. Wixforth, C. Gorzelanny, A. Alexander-Katz, R. R. Netz, and M. F. Schneider, Shear-induced unfolding triggers adhesion of von Willebrand factor fibers. *Proc. Nat. Acad. Sci.* **104** (2007), 7899–7903.

53. L. Shi, T.-W. Pan, and R. Glowinski, Three-dimensional numerical simulation of red blood cell motion in Poiseuille flows, *International Journal for Numerical Methods in Fluids* **76** (2014), 397–415.

54. S. Shimizu, D. Une, T. Kawada, Y. Hayama, A. Kamiya, T. Shishido, and M. Sugimachi, Lumped

parameter model for hemodynamic simulation of congenital heart diseases. *The Journal of Physiological Sciences* **68** (2017), 103–111.

55. S. S. Simakov, Lumped parameter heart model with valve dynamics. *Russian Journal of Numerical Analysis and Mathematical Modelling* **34** (2019), 289–300.

56. T. A. Springer, Von Willebrand factor, Jedi knight of the bloodstream. *Blood* **124** (2014), 1412–1425.

57. F. Sterpone, P. Derreumaux, and S. Melchionna, Protein simulations in fluids: coupling the OPEP coarse-grained force field with hydrodynamics. *Journal of Chemical Theory and Computation* **11** (2015), 1843–1853.

58. S. Succi, *The Lattice Boltzmann Equation for Fluid Dynamics and Beyond (Numerical Mathematics and Scientific Computation)*. Oxford University Press, USA, 2001.

59. A. A. Tokarev, A. A. Butylin, and F. I. Ataullakhanov, Platelet adhesion from shear blood flow is controlled by near-wall rebounding collisions with erythrocytes. *Biophysical Journal* **100** (2011), 799–808.

60. A. A. Tokarev, A. A. Butylin, E. A. Ermakova, E. E. Shnol, G. P. Panasenko, and F. I. Ataullakhanov, Finite platelet size could be responsible for platelet margination effect. *Biophysical Journal* **101** (2011), 1835–1843.

61. A. Tosenberger, F. Ataullakhanov, N. Bessonov, M. Panteleev, A. Tokarev, and V. Volpert, Modelling of thrombus growth in flow with a DPD-PDE method. *Journal of Theoretical Biology* **337** (2013), 30–41.

62. R. Tran-Son-Tay, S. P. Sutera, and P. R. Rao, Determination of red blood cell membrane viscosity from rheoscopic observations of tank-treading motion. *Biophys. J.* **46** (1984), 65–72.

63. K. Tsubota, Elongation deformation of a red blood cell under shear flow as stretch testing. *Journal of the Mechanics and Physics of Solids* **152** (2021), 104345.

64. N. G. Tsyu and A. V. Belyaev, Coarse-grained simulations of von Willebrand factor adsorption to collagen with consequent platelet recruitment. *International Journal for Numerical Methods in Biomedical Engineering* **39** (2023), No. 11, e3747.

65. Yu. V. Vassilevski, S. S. Simakov, T. M. Gamilov, V. Yu. Salamatova, T. K. Dobroserdova, G. V. Kopytov, O. N. Bogdanov, A. A. Danilov, M. A. Dergachev, D. D. Dobrovolskii, O. N. Kosukhin, E. V. Larina, A. V. Meleshkina, E. Yu. Mychka, V. Yu. Kharin, K. V. Chesnokova, and A. A. Shipilov, Personalization of mathematical models in cardiology: obstacles and perspectives. *Computer Research and Modeling* **14** (2022), 911–930.

66. V. Voevodin, A. Antonov, D. Nikitenko, P. Shvets, S. Sobolev, I. Sidorov, K. Stefanov, V. Voevodin, and S. Zhumatiy, Supercomputer Lomonosov-2: large scale, deep monitoring and fine analytics for the user community. *Supercomputing Frontiers and Innovations* **6** (2019), 4–11.

67. W. Yao, Z. Wen, Z. Yan, D. Sun, W. Ka, L. Xie, and S. Chien, Low viscosity ektacytometry and its validation tested by flow chamber. *Journal of Biomechanics* **34** (2001), 1501–1509.

68. G. Zavodszky, B. van Rooij, V. Azizi, and A. Hoekstra, Cellular level in-silico modeling of blood rheology with an improved material model for red blood cells. *Frontiers in Physiology* **8** (2017).